Coherent detection of THz-induced sideband emission from excitons in the nonperturbative regime

K. Uchida,[1] T. Otobe,[2] T. Mochizuki,[3] C. Kim,[4] M. Yoshita,[3] K. Tanaka,[1,5] H. Akiyama,[4,6]
L. N. Pfeiffer,[7] K. W. West,[7] and H. Hirori[5,8,*]

[1]*Department of Physics, Graduate School of Science, Kyoto University, Kyoto, Kyoto 606-8502, Japan*
[2]*Kansai Photon Science Institute, National Institutes for Quantum and Radiological Science and Technology, Kizugawa, Kyoto 619-0615, Japan*
[3]*Fukushima Renewable Energy Institute, National Institute of Advanced Industrial Science and Technology, Koriyama, Fukushima 963-0298, Japan*
[4]*Institute for Solid State Physics, University of Tokyo, Kashiwa, Chiba 277-8581, Japan*
[5]*Institute for Integrated Cell-Material Sciences (iCeMS), Kyoto University, Kyoto, Kyoto 606-8501, Japan*
[6]*AIST-UTokyo OPERANDO-OIL, University of Tokyo, Kashiwa, Chiba 277-8589, Japan*
[7]*Department of Electrical Engineering, Princeton University, Princeton, New Jersey 08544, USA*
[8]*Institute for Chemical Research, Kyoto University, Uji, Kyoto 611-0011, Japan*

(Received 27 December 2017; published 13 April 2018)

Strong interaction of a terahertz (THz) wave with excitons induces nonperturbative optical effects such as Rabi splitting and high-order sideband generation. Here, we investigated coherent properties of THz-induced sideband emissions from GaAs/AlGaAs multiquantum wells. With increasing THz electric field, optical susceptibility of the THz-dressed exciton shows a redshift with spectral broadening and extraordinary phase shift. This implies that the field ionization of the 1*s* exciton modifies the THz-dressed exciton in the nonperturbative regime.

DOI: 10.1103/PhysRevB.97.165122

I. INTRODUCTION

The coherent nonlinear interaction of intense light fields with electronic states in semiconductors gives rise to intriguing nonperturbative phenomena such as high-harmonic generation and optical-field-induced current [1–3], which possess electron dynamics that are highly sensitive to the driving phase of the laser [4]. These dynamics are characterized by light-matter interaction energy such as Rabi energy $\hbar\Omega_R$ and ponderomotive energy U_p. Rabi energy $\hbar\Omega_R$ describes coupling strength between electronic state and light, and ponderomotive energy describes the time-averaged kinetic energy of an electron under a light field. When such light-matter interaction energies approach the same order of magnitude as the transition energy of an electronic state, the rotating-wave approximation (RWA) and perturbation theory cannot be applied [5]. Excitons in semiconductors, which are hydrogenlike quasiparticles scaled energetically by 1/1000 compared with atomic systems, are attractive for studying the light-matter interactions in the presence of Coulomb interactions [6]. The intraexcitonic transitions have a large dipole moment and their energies lie in the terahertz (THz) range [7]. These properties allow us to reach a highly nonperturbative regime ($\hbar\Omega_R$, $U_p \sim \varepsilon_{1s-2p}$: transition energy of exciton) with comparably moderate fields without breakdown of material.

Recent studies on the interactions between excitons and THz electric fields have revealed the Rabi splitting [8–10], the electric-field-induced ionization [11,12], and the sideband emission [13–15]. In previous work, the excitonic optical absorption of semiconductors in the presence of a THz wave has been modulated on a subcycle timescale [16,17]. We found that the output probe intensity was coherently reshaped by the sideband emissions from the THz-photon-dressed state of the exciton [17,18]. The modulation can be explained by the optical susceptibility which involves the energy spectrum of the THz-dressed excitons [19]. In the nonperturbative regime, it is well known that the THz electric field induces excitonic ionization and high-order sideband generation (HSG) [15,16]. As the ionization may modify the THz-dressed excitons, it is crucial to determine the dependence of the susceptibility on the field strength for a deeper understanding of the HSG in the nonperturbative regime, which is useful for subcycle control and synthesis of optical pulses.

In this study, by using a heterodyne detection technique, we investigated the coherent properties of the sideband emission from excitons and obtained the optical susceptibility under intense THz wave illumination, which is directly related to the energy spectrum of the THz-dressed excitons. The ground-state (1*s*) excitons in a GaAs/AlGaAs multiquantum well (MQW) were excited by near-infrared (NIR) pulses and driven via phase-stable multicycle THz pulses. The dependence of both the amplitude and phase of the second-order sideband emission on the THz electric field implies that the field ionization of the 1*s* exciton strongly modifies the energy spectrum of the dressed exciton.

II. EXPERIMENT

A. Setup and sample

In our experiment, we utilized a THz electric field to drive the intraexcitonic transition in a GaAs/AlGaAs MQW and a NIR pulse which excites the exciton (exc-NIR pulse), and observed the sideband emissions from the MQW sample as

*hirori@scl.kyoto-u.ac.jp

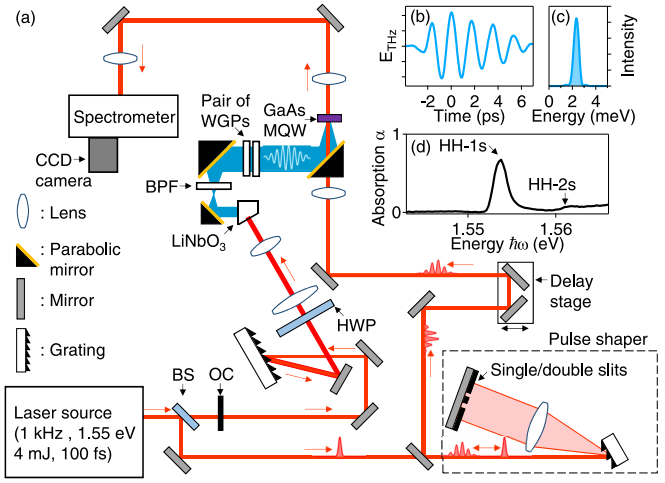

FIG. 1. (a) Experimental setup for coherent detection of THz-induced sideband emissions from a GaAs/AlGaAs MQW. The NIR pulse passed through a small hole in the parabolic mirror used to focus the THz waves. Both polarizations of the THz and NIR waves were linear and parallel. BS: nonpolarized beam splitter, OC: optical chopper, HWP: half-wave plate, BPF: bandpass filter (0.6 THz). (b) Temporal profile of the THz electric field measured by electro-optic sampling with a 400-μm-thick GaP crystal. (c) Fourier amplitude spectrum of the THz wave. (d) Absorption spectrum of the GaAs/AlGaAs MQW at 10 K defined as $-\log(I_{\rm sam}/I_{\rm ref})$, where $I_{\rm sam}$ and $I_{\rm ref}$ are transmitted intensities with and without sample. The background term due to the multiple reflections within the sample is excluded. HH indicates a heavy-hole exciton.

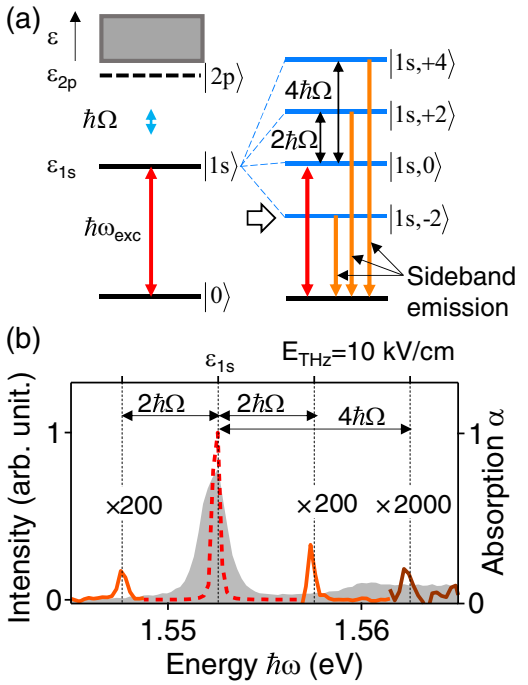

FIG. 2. (a) Schematics of the excitonic energy states (left) and the sideband emissions from the THz-dressed exciton (right). The 1s and 2s exciton states lie below the higher excitonic and continuum states (gray-shaded area). (b) Sideband spectrum under THz wave illumination with $E_{\rm THz} = 10\,{\rm kV/cm}$. The red dashed line is the incident NIR spectrum that was narrowed by the pulse shaper with a single slit. The orange and brown solid lines indicate the spectra of three sideband emissions ($\pm$2nd and +4th order, respectively). The vertical scales are, respectively, multiplied by 200 and 2000. The gray-shaded area shows absorption spectrum.

illustrated in Fig. 1(a). The laser source was a Ti:sapphire regenerative amplifier (repetition rate: 1 kHz, pulse energy: 4 mJ, central energy: 1.55 eV, pulse width: 100 fs). The NIR laser output was split to generate the NIR pulses and the THz driving pulses with two separate beam paths. Single-cycle THz pulses were generated with a $LiNbO_3$ crystal by using the tilted-pulse-intensity-front scheme and we converted them into multicycle (narrow-band) ones by using a bandpass filter [20,21]. Figures 1(b) and 1(c) show the temporal and the Fourier profiles of the THz pulse with a central energy of $\hbar\Omega = 2.5\,{\rm meV}$ ($\Omega = 0.6\,{\rm THz}$) and a bandwidth of 0.4 meV (0.1 THz). A pair of wire grid polarizers (WGPs) was used to vary the amplitude of the THz electric field from 0.4 to 16 kV/cm without changing its temporal profile. The NIR pulses were passed through a pulse shaper consisting of a grating, lens, and a single-slit mask to obtain a narrow-band and wavelength-tunable exc-NIR pulse (see Sec. II B). When a double-slit mask is inserted in the pulse shaper, two NIR pulses with different color are obtained, and the high-energy photons can be used as a reference (ref-) pulse in the heterodyne detection explained later (see Sec. II C). The NIR pulses that were transmitted through the sample were analyzed by a spectrometer with an energy resolution of 0.3 meV and detected with a charge-coupled-device camera.

In our experiment, we used a GaAs/AlGaAs MQW sample that consisted of ten periods of 12-nm-wide GaAs wells separated by 10-nm-wide $Al_{0.3}Ga_{0.7}As$ barriers grown on a semi-insulating GaAs (100) substrate with molecular-beam epitaxy. To enable optical transmission measurements, the GaAs substrate was removed by chemical etching and attached to a SiO_2 substrate. The sample was placed in a cryostat and the temperature during the experiments was set to 10 K. Figure 1(d) shows the absorption spectrum of the GaAs/AlGaAs MQW at 10 K. The dominant peak at $\varepsilon_{1s} = 1.55\,{\rm eV}$ is attributed to the 1s state of the heavy-hole (HH) exciton. From the 2s-HH exciton peak observed at higher energies, the 1s-2p transition energy ε_{1s-2p} is estimated to be 8 meV, which is larger than $\hbar\Omega$ and thus we have a nonresonant driving of the excitonic system in our experiment.

B. Measurement of the sideband emission intensity

The schematic energy diagram of the excitonic system without THz illumination is shown on the left-hand side in Fig. 2(a), and the right-hand side illustrates the THz-dressed excitonic system caused by the THz wave illumination. The eigenstates of the dressed exciton are separated by even multiples of the THz photon energy $\hbar\Omega$ ($\varepsilon_{1s} + 2n\hbar\Omega$, with n being an integer). When the dressed exciton is excited by the exc-NIR pulse with the energy of $\hbar\omega_{\rm exc}$, the THz-induced 2mth-order sideband (hereafter referred to as 2mth sideband) emissions can be observed ($\hbar\omega_{\rm exc} + 2m\hbar\Omega$, with m being an integer). Figure 2(b) shows the sideband spectrum obtained for simultaneous excitation with the exc-NIR pulse ($\hbar\omega_{\rm exc}$ resonant with $\varepsilon_{1s} = 1.55\,{\rm eV}$) and the

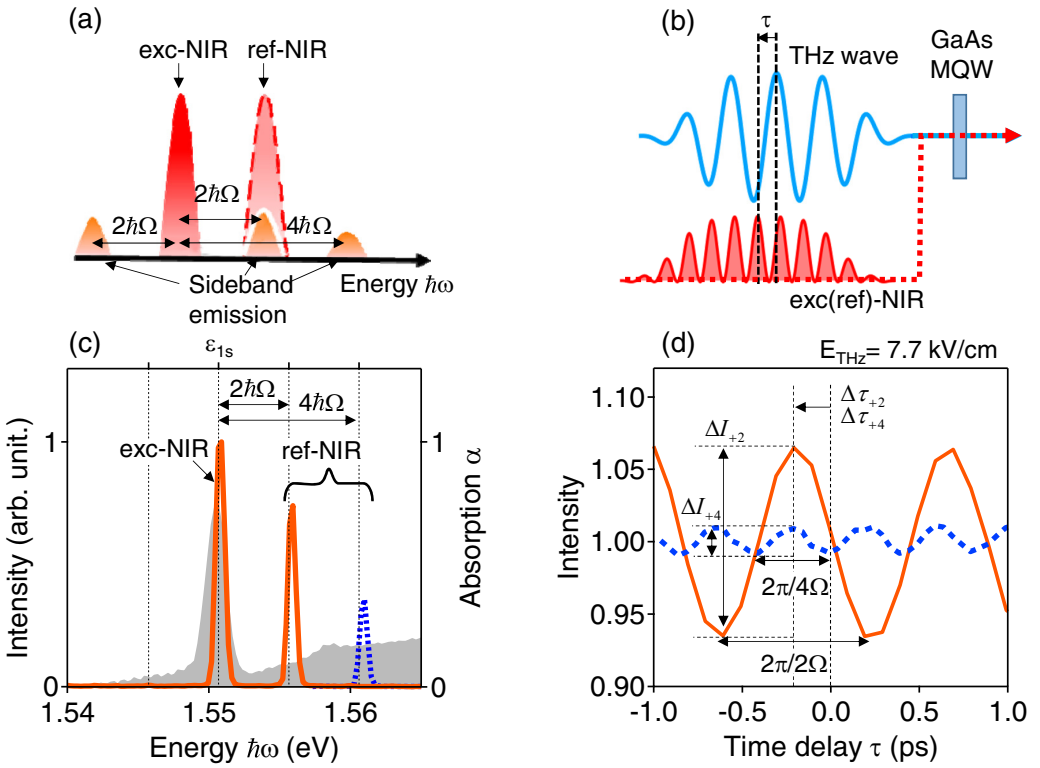

FIG. 3. (a) Schematic diagram of coherent sideband detection in the frequency domain exc- and ref- indicates the NIR waves that were used for the excitation of the system and the reference for the heterodyne detection, respectively. (b) Schematic diagram of coherent sideband detection in the time domain. The beating frequency of the NIR pulse corresponds to the energy separation between the exc- and ref-NIR wave in (a). The time delay τ between the THz and NIR pulses is defined as the difference between the peak positions of the THz electric field and the NIR pulse in the time domain. (c) NIR transmission spectra obtained for energy separations set to $2\hbar\Omega$ (orange solid line) and $4\hbar\Omega$ (blue dashed line). The gray area shows the absorption spectrum. (d) Transmitted NIR intensities as a function of delay time τ at $E_{\mathrm{THz}} = 7.7\,\mathrm{kV/cm}$. The orange solid and blue dashed lines correspond to the NIR signal intensities shown in (c). ΔI_{2m} and $\Delta\tau_{2m}$ ($2m = +2$ and $+4$) are modulation depth and time lag of the signal peak of the $2m$th sideband emission, respectively. Intensities are normalized by the respective time-averaged intensities over the cycle of THz wave $2\pi/\Omega$.

THz wave ($E_{\mathrm{THz}} = 10\,\mathrm{kV/cm}$). The orange solid lines are the three emission peaks of the $\pm$2nd and +4th sideband.

In our experiment, the field strength of exc-NIR pulse E_{exc} is sufficiently weak, and thus the complex electric-field amplitude of the $2m$th sideband emission E_{2m} is linearly proportional to the field E_{exc}, and can be described in the frequency domain with

$$E_{2m}(\omega_{\mathrm{exc}} + 2m\Omega) = C_{2m}(\omega_{\mathrm{exc}}, E_{\mathrm{THz}}, \Omega) E_{\mathrm{exc}}(\omega_{\mathrm{exc}}). \quad (1)$$

Here, the complex coefficient $C_{2m}(\omega_{\mathrm{exc}}, E_{\mathrm{THz}}, \Omega)$ is proportional to the optical susceptibility $\chi_{2m}(\omega_{\mathrm{exc}})$ under THz wave illumination, and is directly related to the energy spectrum of the THz-dressed exciton [18]. The components of $C_{2m} = |C_{2m}|\exp(i\theta_{2m})$ reflect the amplitude ratio ($|C_{2m}| = |E_{2m}/E_{\mathrm{exc}}|$) and phase difference ($\theta_{2m}[= \arg(E_{2m}/E_{\mathrm{exc}})]$) between the $2m$th sideband emission and the exc-NIR pulse. The squared amplitude $|C_{2m}|^2$ indicates sideband intensity efficiency, and can be estimated from the intensity of the sideband emission as shown in Fig. 2(b), e.g., $|C_{+2}|^2 \approx 10^{-3}$ at a THz electric-field strength of 10 kV/cm. However, we cannot access the phase information θ_{2m} with this simple measurement.

C. Heterodyne detection technique

In order to access the complex coefficient C_{2m} of the $2m$th sideband emission with high sensitivity, we utilized a heterodyne detection technique. By using a double-slit mask in the pulse shaper, a two-color NIR pulse with photon energies of $\hbar\omega_{\mathrm{exc}}$ and $\hbar\omega_{\mathrm{ref}}$ ($= \hbar\omega_{\mathrm{exc}} + 2m\hbar\Omega$) can be produced as depicted in Fig. 3(a). The high-energy photons ($\hbar\omega_{\mathrm{ref}}$) were used for the ref-NIR pulse in the heterodyne detection. Here, for simplicity, we assume continuous THz and NIR waves, which can be described by

$$\tilde{E}_{\mathrm{THz}}(t) = \tfrac{1}{2} E_{\mathrm{THz}} \exp(i\Omega t) + \mathrm{c.c.}, \quad (2)$$

$$\tilde{E}_{\mathrm{NIR}}(t) = \tfrac{1}{2}\{E_{\mathrm{exc}} \exp[i\omega_{\mathrm{exc}}(t-\tau)] + E_{\mathrm{ref}} \exp[i(\omega_{\mathrm{exc}} + 2m\Omega)(t-\tau)]\} + \mathrm{c.c.}, \quad (3)$$

where τ is the time delay between the THz and NIR pulses, and E_{ref} is the electric-field amplitude of the ref-NIR pulse. As shown in Fig. 3(b), the time delay τ in Eq. (2) is defined with the time difference between the maximum-peak positions of the THz and NIR pulses.

The ideally transmitted NIR intensity I_{tot} (at $\hbar\omega_{\mathrm{exc}} + 2m\hbar\Omega$) detected after the sample is a combination of the $2m$th sideband emission and the ref-NIR wave. By using Eqs. (1)

and (3), $I_{\rm tot}$ as a function of the time delay τ can be written as

$$\begin{aligned} I_{\rm tot}(\omega_{\rm exc}+2m\Omega,\tau) &\propto |E_{\rm ref}\exp[-i(\omega_{\rm exc}+2m\Omega)\tau] \\ &\quad + C_{2m}E_{\rm exc}\exp[-i\omega_{\rm exc}\tau]|^2 \\ &= E_{\rm ref}^2 + |C_{2m}|^2E_{\rm exc}^2 + 2|C_{2m}|E_{\rm exc}E_{\rm ref} \\ &\quad \times \cos(2m\Omega\tau+\theta_{2m}). \end{aligned} \tag{4}$$

The first and second terms in Eq. (4) correspond to the intensities of the ref-NIR pulse and the $2m$th sideband emission, respectively. The third term expresses the interference between them. By changing the time delay τ, the interference term in Eq. (4) oscillates with a frequency of $2m\Omega$. This technique enables us to obtain the phase of the sideband emission θ_{2m} in addition to the amplitude $|C_{2m}|$. It is important that this heterodyne detection allows us to detect the sideband emission with higher sensitivity, which is explained in the following. Actually, from our measurement shown in Sec. II B, the conversion efficiency of the exc-NIR intensity to the +2nd sideband emission intensity is estimated to be $|C_{+2}|^2 \approx 10^{-3}$ at a THz electric-field strength of 10 kV/cm. On the other hand, the interference signal ratio $2|C_{+2}|$ is as high as 6×10^{-2} for $E_{\rm ref}\approx E_{\rm exc}$, which indicates a more than 10 times larger signal than that obtained with simply measuring the sideband emission intensity ($\sim10^{-3}$).

Figure 3(c) shows the spectra of the incident two-color NIR pulses with the excitation energy set to the $1s$ excitonic resonance ($\hbar\omega_{\rm exc}=\varepsilon_{1s}$). For the heterodyne detection of the +2nd and +4th sideband emissions, we set the energy separation between the exc- and ref-NIR pulses to $2\hbar\Omega$ (orange solid line) and $4\hbar\Omega$ (blue dashed line), respectively. The corresponding transmitted NIR intensities under THz wave illumination ($E_{\rm THz}=7.7$ kV/cm) show clear oscillations when scanning the delay time τ [Fig. 3(d)]. The periods of the orange and blue oscillations are $2\pi/2\Omega$ and $2\pi/4\Omega$, respectively, in accordance with Eq. (4). The modulation strength of $\sim6\times10^{-2}$ for the modulation frequency of 2Ω (orange solid line) is also in good agreement with the estimation from Fig. 2(b). Hence, from the modulation depth ΔI_{2m} and the time lag of the signal peak $\Delta\tau_{2m}$ depicted in Fig. 3(d), we can extract the amplitude $|C_{2m}|$ and the phase θ_{2m} of the $2m$th sideband emission by using the relations $\Delta I_{2m}=4|C_{2m}|(I_{\rm ref}I_{\rm exc})^{1/2}$ and $\Delta\tau_{2m}=\theta_{2m}/2m\Omega$.

III. SIDEBAND EMISSION IN THE NONPERTURBATIVE REGIME

A. Excitation spectra of the +2nd sideband emission

In the following we discuss the +2nd sideband emission (C_{+2}), because this sideband can be clearly observed in both the perturbative and the nonperturbative regimes. To access the properties of the +2nd sideband emission, we performed the heterodyne detection for an energy separation of $2\hbar\Omega=5$ meV between the exc- and ref-NIR pulses as shown in Fig. 4(a). We measured the amplitude spectra of the +2nd sideband emission ($|C_{+2}|$) at two different THz electric fields ($E_{\rm THz}=2.7$ and 16 kV/cm) by scanning the exc- and ref-NIR photon energies ($\hbar\omega_{\rm exc}$, $\hbar\omega_{\rm ref}=\hbar\omega_{\rm exc}-5$ meV) around the $1s$ exciton resonance energy ε_{1s}. Experimentally obtained excitation spectra are shown in Fig. 4(b). The blue circles in Fig. 4(b) show that the amplitude spectrum has a sharp peak near ε_{1s} for a low THz field strength of $E_{\rm THz}=2.7$ kV/cm. At the higher field $E_{\rm THz}=16$ kV/cm, the spectral profile becomes broader and exhibits a redshift of around 2 meV as shown by orange squares in Fig. 4(b) [22], in contrast to what is expected in the perturbation theory, i.e., increase with $E_{\rm THz}^2$ without spectral shape change. At 16 kV/cm, the Rabi energy ($\hbar\Omega_{\rm R}=7$ meV $\propto E_{\rm THz}$) is comparable to the intraexcitonic transition energy $\varepsilon_{1s-2p}=8$ meV, and these energies are much smaller than the ponderomotive energy ($U_{\rm p}=147$ meV $\propto E_{\rm THz}^2$) [23]. Consequently, the interaction between the exciton and THz field causing the spectral shape change at 16 kV/cm [Fig. 4(b)] enters the nonperturbative regime where the RWA and perturbation theory are invalid.

Figure 4(c) plots the cycle-averaged absorption spectra obtained for different $E_{\rm THz}$. Similar to the result observed for the sideband amplitude $|C_{+2}|$ [Fig. 4(b)], the $1s$ exciton absorption shows a significant spectral broadening at $E_{\rm THz}=16$ kV/cm, which can be explained by a reduction of the dephasing time of the THz-dressed $1s$ exciton. The underlying physics of this nonperturbative behavior are discussed below. We found that the absorption spectrum starts to broaden at $E_{\rm THz}=4$ kV/cm, which is evidenced in Fig. 4(d). Interestingly, the static field that is needed to ionize the $1s$ excitons is roughly estimated by $E_{\rm ion}=\varepsilon_{\rm B}/ea_{\rm B}\sim\varepsilon_{1s-2p}/\hbar\Omega_{\rm R}$, resulting in 4 kV/cm [24], which can be calculated when we use $\varepsilon_{\rm B}\sim8$ meV for the binding energy, and $a_{\rm B}\sim20$ nm for the Bohr radius of the $1s$ excitons ($\sim$20 nm), and the elementary charge e. This indicates that the spectral broadening observed in Fig. 4(b) originates from the distortion of the dressed $1s$ exciton due to the strong coupling with the continuum states (ionization).

On the other hand, the energy of the $1s$ excitonic resonance ε_{1s} shows only slight variations as shown in Fig. 4(d). We observed a redshift (<0.3 meV) below 5 kV/cm which is due to the ac Stark effect, and a blueshift (<0.6 meV) which is due to the dynamical Franz-Keldysh effect [25,26]. Since the redshift in absorption (<0.3 meV) is much smaller than that observed for the +2nd sideband amplitude [Fig. 4(b); orange squares, $\sim$2 meV], there is an additional effect on the +2nd sideband emission in the nonperturbative regime.

B. Dressed excitons in the nonperturbative regime

To understand the dressed exciton in the nonperturbative regime, we analyzed the data with the analytical expression for the +2nd sideband amplitude $|C_{+2}|$, which can be defined with [17,19,27]

$$\begin{aligned} C_{+2}(\omega_{\rm exc}) &\propto \chi_{+2}(\omega_{\rm exc}) \\ &= \frac{|P_{\rm CV}|^2}{\varepsilon_0\hbar}\sum_{j,l}\frac{\phi^*_{j,l+2}(0)\phi_{j,l}(0)}{(\omega_{\rm exc}-\varepsilon_j/\hbar-l\Omega)-i\Gamma_j}, \end{aligned} \tag{5}$$

$$\psi_j(\boldsymbol{r},t)=\exp(-i\varepsilon_j t/\hbar)\sum_n\phi_{j,n}(\boldsymbol{r})\exp(-in\Omega t), \tag{6}$$

where ε_0 and $P_{\rm CV}$ are the vacuum permittivity and interband dipole moment, χ_{+2} is the optical susceptibility of the +2nd sideband emission described with the dressed exciton ψ_j of state j (j being 1s, $2s$, $2p$, ...), $\phi_{j,n}$ is the nth sideband state of ψ_j, $\boldsymbol{r}$ indicates the distance between the electron and hole, and ε_j and Γ_j are the quasienergy and the dephasing rate of

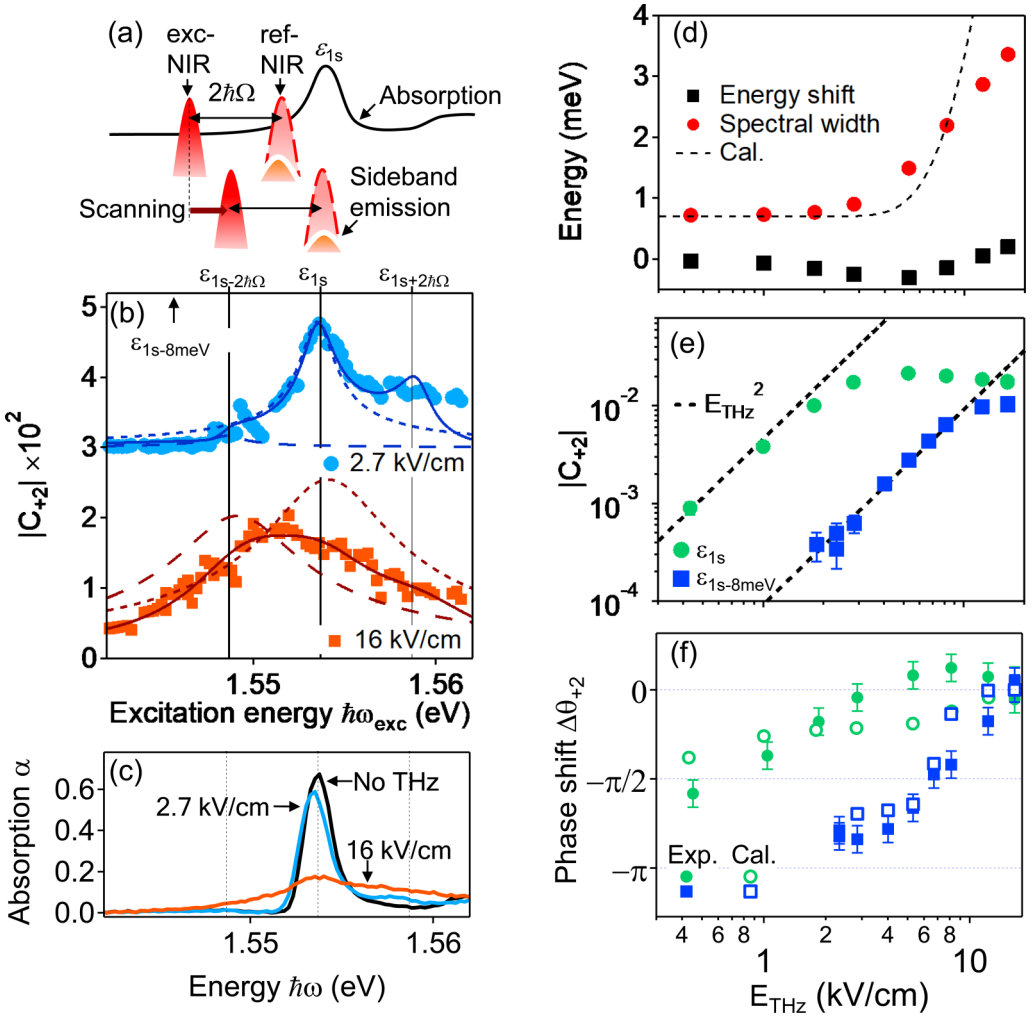

FIG. 4. (a) Schematic diagram of the heterodyne scanning procedure. (b) +2nd-order sideband amplitude spectra $|C_{+2}(\omega_{exc})|$. $\varepsilon_{1s+2\hbar\Omega}$ and $\varepsilon_{1s-2\hbar\Omega}$ indicate the energy of $\varepsilon_{1s}+2\hbar\Omega$ and $\varepsilon_{1s}-2\hbar\Omega$, respectively. The light-blue circles and orange squares are the measurement results obtained for $E_{THz}=2.7$ and 16 kV/cm, respectively. The blue and brown solid lines are the fitting results for $|C_{+2}|$ using Eq. (5). The dotted and dashed lines correspond to $|C_{+2}|$ for $(j,l)=(1s,0)$ and $(1s,-2)$. The data of $|C_{+2}|$ for $(j,l)=(2p,-1)$, which has a peak around $\varepsilon_{1s+2\hbar\Omega}$, are not shown in the graph. (c) Absorption spectra without THz illumination (black solid line), and for THz electric-field strengths of $E_{THz}=2.7$ kV/cm (light-blue solid line), and $=16$ kV/cm (orange solid line). (d) THz field dependence of the peak energy shift (black squares) and spectral width (red circles) of the $1s$ exciton absorption evaluated by Lorentzian fitting. The dashed line is the calculation result of the cycle-averaged field-ionization rate from Ref. [24]. (e) +2nd sideband amplitude $|C_{+2}|$ as a function of E_{THz}. The green circles and blue squares, respectively, indicate measurement results for $\hbar\omega_{exc}=\varepsilon_{1s}$ and $\varepsilon_{1s-8\,meV}$. The black dashed lines are proportional to E_{THz}^2. (f) Phase shift of the +2nd-order sideband emission at $\hbar\omega_{exc}=\varepsilon_{1s}$ and $\varepsilon_{1s-8\,meV}$ (green solid circles and blue solid squares, respectively). Green open circles and blue open squares indicate the phase shift deduced from the fitting results in (b) by using Eq. (5).

j-state exciton under THz wave illumination, respectively. The parameters of $\phi_{j,n}$, ε_j, and Γ_j in Eq. (5) depend on THz electric field, reflecting THz-exciton interactions such as ionization effect on dressed excitons.

Solid curves in Fig. 4(b) are the best-fitted results of excitation spectra using Eq. (5) when we use $\phi^*_{j,l+2}(0)\phi_{j,l}(0)$ as fitting parameter. The fitting reproduces experimental results well in the energy region below the $1s$ excitonic resonance for both $E_{THz}=2.7$ and 16 kV/cm. In the fitting calculation, we considered the dressed states of the $1s$ and $2p$ exciton ($j=1s$ and $2p$) with n ranging from -2 to 2, corresponding to $(j,l)=(1s,0),(1s,-2)$, and $(2p,-1)$ in Eq. (5), which are main contributions in the perturbative regime [17]. Also, ε_{1s} and Γ_{1s} are set to the values estimated by the fitting of the absorption spectra in Fig. 4(c), and assumed as $\varepsilon_{2p}=\varepsilon_{1s}+8$ meV and $\Gamma_{2p}=\Gamma_{1s}$. The fitting errors above $\varepsilon_{1s}+2\hbar\Omega$ can be attributed to the lack of contributions of higher-order excitonic and continuum state. The contributions of $(j,l)=(1s,-2)$ and $(1s,0)$ in Eq. (5) are, respectively, proportional to $\phi^*_{1s,0}(0)\phi_{1s,-2}(0)$ and $\phi^*_{1s,2}(0)\phi_{1s,0}(0)$, whose signs are opposite each other for the perturbation calculation result with $\hbar\Omega<\varepsilon_{1s-2p}$ [17]. Thus, we can evaluate the ratio between $\phi_{1s,-2}(0)$ and $\phi_{1s,2}(0)$. At $E_{THz}=2.7$ kV/cm, the value of $|\phi_{1s,-2}(0)|$ is much smaller than $|\phi_{1s,2}(0)|(|\phi_{1s,-2}(0)/\phi_{1s,2}(0)|\sim0.1)$. But, it becomes comparable to $|\phi_{1s,2}(0)|$ at $E_{THz}=16$ kV/cm ($|\phi_{1s,-2}(0)/\phi_{1s,2}(0)|\sim0.8$), meaning that the amplitude of the term which includes $\phi_{1s,-2}(0)$ in Eq. (5) [indicated by the yellow dashed line in Fig. 4(b)] becomes close to the term

$\phi_{1s,2}(0)$ [the red dotted line in Fig. 4(b)] in the nonperturbative regime [7]. Since the peak energy of the term $\phi_{1s,-2}(0)$ is lower than that of $\phi_{1s,2}(0)$ by $2\hbar\Omega = 5$ meV, the peak energy of the total sideband amplitude spectrum $|C_{+2}|$ becomes redshifted [the solid square and line in Fig. 4(b); ~2 meV] and larger than that seen in absorption [Figs. 4(c) and 4(d); <0.3 meV].

The THz-exciton interaction term $\hbar\Omega_R(t) = dE_{THz}(t) = dE_{THz}\cos(\Omega t)$ (instantaneous Rabi energy) can be split into two terms, which are, respectively, proportional to $\exp(-i\Omega t)$ and $\exp(i\Omega t)$. These, respectively, correspond to co- and counter-rotating terms for $1s$ exciton. RWA is the approximation which neglects the counter-rotating term, and is valid when THz excitation is resonant to the $1s$-$2p$ transition. Hence, $\phi_{1s,-2}(\boldsymbol{r})$, which is due to the counter-rotating term, should be negligible compared with $\phi_{1s,2}(\boldsymbol{r})$, which is due to the corotating term. Although our experimental condition is not resonant to $1s$-$2p$ transition ($\varepsilon_{1s-2p} = 8$ meV $> \hbar\Omega =$ 2.5 meV), the perturbation calculation result for the two-level ($1s$ and $2p$ exciton) model shows that $|\phi_{1s,2}(0)|/|\phi_{1s,-2}(0)|$ is given by $(\varepsilon_{1s-2p} + \hbar\Omega)/(\varepsilon_{1s-2p} - \hbar\Omega) > 1$ [17]. Our experimental results at 2.7 kV/cm in Fig. 4(b) shows $|\phi_{1s,-2}(0)| < |\phi_{1s,2}(0)|$. In contrast, $|\phi_{1s,-2}(0)|$ is almost the same as $|\phi_{1s,2}(0)|$ at 16 kV/cm, meaning that the RWA is invalid in the nonperturbative regime we studied.

Figure 4(e) shows the THz electric-field dependences of the sideband amplitude $|C_{+2}|$ at ε_{1s} and $\varepsilon_{1s-8\,\mathrm{meV}}$ ($= \varepsilon_{1s} - 8.0$ meV). At ε_{1s}, where the contribution from $|\phi_{1s,2}(0)|$ is dominant, the amplitude starts to deviate from the power law ($\propto E_{THz}^2$) for THz fields above $E_{THz} = 3$ kV/cm, which is almost the same field strength for ionization of the $1s$ exciton. On the other hand, at $\varepsilon_{1s-8\,\mathrm{meV}}$, where the contribution of $|\phi_{1s,-2}(0)|$ is relatively strong, the amplitude obeys the power law up to 10 kV/cm. Since the energy of $\phi_{1s,2}(\boldsymbol{r})$ (i.e., $\varepsilon_{1s} + 2\hbar\Omega$) is closer to the continuum than that of $\phi_{1s,-2}(\boldsymbol{r})$ ($\varepsilon_{1s} - 2\hbar\Omega$), the field-ionization effect is more pronounced for $\phi_{1s,2}(\boldsymbol{r})$, and this causes the saturation of $|\phi_{1s,2}(0)|$ at high THz fields ($|\phi_{1s,2}(0)| \sim |\phi_{1s,-2}(0)|$). Figure 4(f) plots the phase shift $\Delta\theta_{+2}$ of the +2nd sideband emission at ε_{1s} and $\varepsilon_{1s-8\,\mathrm{meV}}$ as a function of E_{THz}. Here, the phase shift is defined with $\Delta\theta_{+2}(E_{THz}) = \theta_{+2}(E_{THz}) - \theta_{+2}(E_{THz} = 16\,\mathrm{kV/cm})$. Below 5 kV/cm, the phase of the sideband signal at $\varepsilon_{1s-8\,\mathrm{meV}}$ exhibits a shift close to π, i.e., sign inversion of the sideband emission. On the other hand, the phase for the signal at ε_{1s} is less sensitive to the THz electric field. The phase shifts evaluated from the fitting with Eq. (5) [Fig. 4(f); open circles and open squares correspond to ε_{1s} and $\varepsilon_{1s-8\,\mathrm{meV}}$, respectively] reproduce the direct experimental results and confirm the validity of our model, i.e., the relative increase of the amplitude of $\phi_{1s,-2}(0)$, whose sign is opposite that of $\phi_{1s,-2}(0)$, is responsible for the observed sideband emission properties in the nonperturbative regime [28].

IV. SUMMARY

In summary, we investigated the sideband emissions in the nonperturbative regime. We demonstrated that the heterodyne detection of the sideband emission is a powerful tool to access the optical susceptibility of the THz-dressed exciton. The dependences of the +2nd sideband emission on the THz electric-field strength revealed that the field ionization of the $1s$ excitons causes a change in the energy spectrum of the THz-dressed exciton, which is related to reduction of the dephasing time and breakdown of RWA in the nonperturbative regime. The further understanding of the nonperturbative nonlinear optical processes including phase information paves the way for subcycle control and synthesis of optical pulses.

ACKNOWLEDGMENTS

This study was supported by PRESTO Grant No. JPMJPR1427 from JST, Grant-in-Aid for JSPS fellows (Grant No. 17J09419), KAKENHI (Grants No. 26286061, No. 17H06228, No. 26247052, No. 17H06124, and No. 15H03968) from JSPS, and also by NEDO and APSA. The work at Princeton University was also funded by the Gordon and Betty Moore Foundation through the EPiQSIinitiative Grant No. GBMF4420, and by the National Science Foundation MRSEC Grant No. DMR-1420541.

[1] F. Krausz and M. I. Stockman, Nat. Photon. **8**, 205 (2014).
[2] W. Kuehn, P. Gaal, K. Reimann, M. Woerner, T. Elsaesser, and R. Hey, Phys. Rev. Lett. **104**, 146602 (2010).
[3] S. Ghimire, A. D. DiChiara, E. Sistrunk, P. Agostini, L. F. DiMauro, and D. A. Reis, Nat. Phys. **7**, 138 (2011).
[4] A. Schiffrin, T. Paasch-Colberg, N. Karpowicz, V. Apalkov, D. Gerster, S. Mühlbrandt, M. Korbman, J. Reichert, M. Schultze, S. Holzner, J. V. Barth, R. Kienberger, R. Ernstorfer, V. S. Yakovlev, M. I. Stockman, and F. Krausz, Nature (London) **493**, 70 (2013).
[5] M. Wegener, *Extreme Nonlinear Optics* (Springer-Verlag, Berlin, 2005).
[6] H. Haug and S. W. Koch, *Quantum Theory of the Optical and Electronic Properties of Semiconductors* (World Scientific, Singapore, 2009).
[7] R. A. Kaindl, M. A. Carnahan, D. Hägele, R. Lövenich, and D. S. Chelma, Nature (London) **423**, 734 (2003).
[8] S. G. Carter, V. Birkedal, C. S. Wang, L. A. Coldren, A. V. Maslov, D. S. Citrin, and M. S. Sherwin, Science **310**, 651 (2005).
[9] M. Wagner, H. Schneider, D. Stehr, S. Winnerl, A. M. Andrews, S. Schartner, G. Strasser, and M. Helm, Phys. Rev. Lett. **105**, 167401 (2010).
[10] K. Uchida, H. Hirori, T. Aoki, C. Wolpert, T. Tamaya, K. Tanaka, T. Mochizuki, C. Kim, M. Yoshita, H. Akiyama, L. N. Pfeiffer, and K. W. West, Apply. Phys. Lett. **107**, 221106 (2015).
[11] H. Hirori, M. Nagai, and K. Tanaka, Phys. Rev. B **81**, 081305(R) (2010).
[12] B. Ewers, N. S. Köster, R. Woscholski, M. Koch, S. Chatterjee, G. Khitrova, H. M. Gibbs, A. C. Klettke, M. Kira, and S. W. Koch, Phys. Rev. B **85**, 075307 (2012).
[13] J. Kono, M. Y. Su, T. Inoshita, T. Noda, M. S. Sherwin, S. J. Allen, Jr., and H. Sakaki, Phys. Rev. Lett. **79**, 1758 (1997).

[14] M. Wagner, H. Schneider, S. Winnerl, M. Helm, T. Roch, A. M. Andrews, S. Schartner, and G. Strasser, Appl. Phys. Lett. **94**, 241105 (2009).

[15] B. Zaks, R. B. Liu, and M. S. Sherwin, Nature (London) **483**, 580 (2012).

[16] F. Langer, M. Hohenleutner, C. P. Schmid, C. Poellmann, P. Nagler, T. Korn, C. Schüller, M. S. Sherwin, U. Huttner, J. T. Steiner, S. W. Koch, M. Kira, and R. Huber, Nature (London) **533**, 225 (2016).

[17] K. Uchida, T. Otobe, T. Mochizuki, C. Kim, M. Yoshita, H. Akiyama, L. N. Pfeiffer, K. W. West, K. Tanaka, and H. Hirori, Phys. Rev. Lett. **117**, 277402 (2016).

[18] T. Otobe, Y. Shinohara, S. A. Sato, and K. Yabana, Phys. Rev. B **93**, 045124 (2016).

[19] K. Johnsen and A. P. Jauho, Phys. Rev. Lett. **83**, 1207 (1999).

[20] K. -L. Yeh, M. C. Hoffmann, J. Hebling, and K. A. Nelson, Appl. Phys. Lett. **90**, 171121 (2007).

[21] H. Hirori, A. Doi, F. Blanchard, and K. Tanaka, Appl. Phys. Lett. **98**, 091106 (2011).

[22] B. Zaks, H. Banks, and M. S. Sherwin, Appl. Phys. Lett. **102**, 012104 (2013).

[23] We use envelope Rabi energy $\hbar\Omega_{\mathrm{R}} = dE_{\mathrm{THz}}$, which characterizes response of dressed exciton within RWA. Here, d is the transition dipole moment of the $1s$-$2p$ transition, and we used $d = 43\,e$Å, which has been theoretically estimated from the two-dimensional exciton model [see Ref. [6] and M. Shinada and S. Sugano, J. Phys. Soc. Jpn. **21**, 1936 (1966)]. The ponderomotive energy U_{p} is defined as $U_p = e^2E^2_{\mathrm{THz}}/4m^*\Omega^2$, where e is the elementary charge, $m^*(= 0.054m_0)$ is the reduced mass of the exciton, and m_0 is the free-electron mass. The ratio between U_{p} and binding energy of a bounded state ε_{B} given by $\mathrm{KP} = \sqrt{\varepsilon_{\mathrm{B}}/2U_{\mathrm{p}}}$, where KP is the Keldysh parameter (see Ref. [5]). When KP becomes smaller than 1, ionization is described as a tunneling process instead of a multiphoton process.

[24] D. A. B. Miller, D. S. Chemla, T. C. Damen, A. C. Gossard, W. Wiegmann, T. H. Wood, and C. A. Burrus, Phys. Rev. B **32**, 1043 (1985).

[25] K. B. Nordstrom, K. Johnsen, S. J. Allen, A. P. Jauho, B. Birnir, J. Kono, T. Noda, H. Akiyama, and H. Sakaki, Phys. Rev. Lett. **81**, 457 (1998).

[26] M. Teich, M. Wagner, D. Stehr, H. Schneider, M. Helm, C. N. Böttge, A. C. Klettke, S. Chatterjee, M. Kira, S. W. Koch, G. Khitrova, and H. M. Gibbs, Phys. Rev. B **89**, 115311 (2014).

[27] J. H. Shirley, Phys. Rev. **138**, B979 (1965).

[28] By using $\phi^*_{j,l+2}(0)\phi_{j,l}(0)$, ε_j, and Γ_j deduced from the experimental results [Fig. 4(d)], we calculated phase of 2nd sideband emission $\theta_{+2} = \arg(C_{+2})$. Here, in order to interpolate THz electric-field dependence of $\phi^*_{j,l+2}(0)\phi_{j,l}(0)$, we assumed $\phi^*_{1s,2}(0)\phi_{1s,0}(0) = AC_{+2}(\varepsilon_{1s})/\Gamma_{1s}$ and $\phi^*_{1s,0}(0)\phi_{1s,-2}(0) = BC_{+2}(\varepsilon_{1s-8\ \mathrm{meV}})/\Gamma_{1s}$ according to Eq. (5). By using experimentally obtained Γ_{1s}, $|C_{+2}(\varepsilon_{1s})|$, $C_{+2}(\varepsilon_{1s+8\ \mathrm{meV}})|$, and adjusting scales A and B, we obtained THz electric-field dependence of $\phi^*_{i,l+2}(0)\phi_{i,l}(0)$ for the whole range, which is in good agreement with that extracted from the fitting in Fig. 4(b) [THz electric-field dependence of $\phi^*_{2p,1}(0)\phi_{2p,-1}(0)$ is deduced from the linear interpolation].